Thermo-Optical Switches Based on Spin-Crossover Molecules with Wideband Transparency

Lijun Zhang, Jesukpego Anorld Capo Chichi, Stéphane Calvez, Yuteng Zhang, L. Salmon, Gábor Molnár, Karl Ridier, Azzedine Bousseksou

ADVANCED OPTICAL MATERIALS
www.advopticalmat.de

Thermo-Optical Switches Based on Spin-Crossover Molecules with Wideband Transparency

Lijun Zhang, Jesukpego Anorld Capo Chichi, Stéphane Calvez, Yuteng Zhang, Lionel Salmon, Gábor Molnár, Karl Ridier, and Azzedine Bousseksou**

In this work, a thermally tunable optical resonator operating in the visible wavelength range is reported, which consists of a bilayer structure composed of a thin silver layer and a dielectric coating of [Fe(HB(1,2,4-triazol-1-yl)$_3$)$_2$] switchable spin-crossover (SCO) molecules. White light is coupled to the resonant structure using a prism and the resulting resonance spectra are investigated as a function of the incident angle and temperature. Switching the SCO molecules from the low-spin to the high-spin state gives rise to a substantial blueshift of the resonances reaching up to 30 nm (associated with a reflectance modulation of up to 70%), which can be linked, through transfer-matrix simulations, to the variation of the optical thickness of the molecular layer. Interestingly, the study demonstrated that the large thermal tunability of the device also gives rise to a photothermal nonlinearity, which can be leveraged for achieving optical limiting applications. Overall, through the present study, it is shown that molecular SCO nanomaterials can be superior to commonly used thermo-optical switches and well-established optical phase-change materials for applications requiring high broadband optical transparency in the visible spectral domain.

1. Introduction

In the vast fields of optics and photonics, tunability, reconfigurability, and adaptability are major assets, which are highly demanded for various applications.[1,2] These include, for example, displays, optical memories, spatial light modulators (SLMs), photonic integrated circuits (PICs), optical neural networks, and other approaches for optical computing. Notably, there has been recently an explosion of interest in active functionalities for a controlled modification of the phase and/or the amplitude of optical wavefronts in SLMs (e.g., beam steering, holographic displays, distortion correction),[3] or for routing light through PICs (e.g., optical switches, modulators, filters, limiters).[4] Fundamentally, there are two ways to achieve active or adaptive optical properties, which comprise i) changing the geometry of the structure by mechanical displacement(s) (e.g., micro mirrors, deformable mirrors), and ii) using materials with controllable refractive indices. The latter strategy calls, self-evidently, for materials displaying large changes in their dielectric function in response to an external stimulus (e.g., heat, voltage bias, or light irradiation). This is readily observed in a number of materials exhibiting electro/thermo/photo-refractive properties (e.g., liquid crystals, semiconductors, Pockels-effect materials).

More recently, particular attention has been dedicated to compounds, which undergo electronic and/or structural phase transitions, referred to as phase-change materials (PCMs).[5–11] Among the different families of all-solid PCMs, the technologically most prevalent materials are chalcogenide alloys, whose main application field has been rewritable optical storage technology.[12,13] For example, the prototypical PCM chalcogenide alloy, $Ge_2Sb_2Te_5$ (GST), can be switched reversibly from an optically transparent and electrically resistive amorphous state to an optically opaque and electrically conductive crystalline state. The two states are nonvolatile as switching in both directions requires energy input, which can be achieved by heating the material with current or laser pulses to different temperatures (≈150 and 600 °C).[14] This nonvolatility is indispensable for applications in optical memories but becomes an undesirable property in some other applications, such as signal modulation. Alternatively, transition metal oxides displaying metal-insulator transition have been also considered in the "active photonics" context.[15–17] The prime example, VO_2, exhibits concomitant volatile electronic and structural transitions from an optically transparent and electrically insulating monoclinic form to an optically opaque and electrically conducting tetragonal structure at ≈68 °C.[16]

L. Zhang, Y. Zhang, L. Salmon, G. Molnár, K. Ridier, A. Bousseksou
Laboratoire de Chimie de Coordination
CNRS UPR 8241
Université de Toulouse
205 route de Narbonne, Toulouse F-31077, France
E-mail: karl.ridier@lcc-toulouse.fr; azzedine.bousseksou@lcc-toulouse.fr
J. A. Capo Chichi, S. Calvez, Y. Zhang
Laboratoire d'Analyse et d'Architecture des Systèmes
CNRS UPR 8001
Université de Toulouse
7 avenue du colonel Roche, Toulouse F-31400, France

The ORCID identification number(s) for the author(s) of this article can be found under https://doi.org/10.1002/adom.202303252

DOI: 10.1002/adom.202303252

It is important to recognize that the requirements for a PCM are not the same for different photonics applications and a single material cannot meet all specific needs and constraints. Besides the obvious requirement for large refractive index modulation, other potentially important assets comprise i) high refractive index, ii) fast switching speeds in both directions, iii) low energy consumption, iv) good reversibility over a large number of switching cycles, v) processability/integrability and, in some cases, vi) nonvolatility and associated long-time memory-type storage stability. While most of these requirements can be readily fulfilled by the existing (and above-mentioned) PCMs, the experimental device demonstrators have so far been restricted to the near and mid-infrared spectral regions. Indeed, both VO_2 and GST are low-bandgap materials that exhibit high extinction coefficients ($k > 0.5$–1) in at least one of the two phases through the visible and near-infrared (Vis-NIR) spectral ranges.[18] Although some improvements have been recently made to overcome this limitation, for instance by using sulfide and selenide-based chalcogenides (instead of tellurides),[19,20] most of the known PCMs remain unsuitable for operation in the sub-µm-wavelength spectral domain.

In this context, molecular spin-crossover (SCO) materials, which display spin-state switching between the low-spin (LS) and high-spin (HS) electronic configurations of the transition metal ion complex,[21–25] may constitute an attractive family of switchable molecular compounds to design PCM-based photonic devices operating in the Vis-NIR range. Indeed, these compounds exhibit a notable decrease of the refractive index, $\Delta n = n_{LS} - n_{HS} \approx 0.01$–0.1, in broad spectral ranges, when going from the LS to the HS state.[26–29] This refractive index modulation mainly finds its origin in the large mass density change of the material upon the spin transition, the HS state being always the phase of a larger volume ($\Delta V/V \approx$ 1–20% depending on the SCO compound).[30] Although the refractive index change appears to be moderate compared with other conventional PCMs, SCO materials offer significant advantages such as low losses in the Vis-NIR range in both spin states, low power consumption, the possibility of ultrafast, all-optical modulation, and either volatile or nonvolatile response (depending on the presence/absence of a hysteresis loop in the spin-transition curve).

Up to now, however, only a few studies were dedicated to the refractive index switching of SCO compounds. These investigations aimed either to use photonic principles to detect the occurrence of the SCO phenomenon (*sic* "photonics for SCO") or, the other way around, to utilize the switchable optical properties of SCO molecules in active photonic devices (*sic* "SCO for photonics"). From this perspective, nanometric thin films, nanoparticles, and lithographically-patterned gratings of various SCO materials have been studied using high-sensitivity refractive index sensing methods,[31] such as surface plasmon resonance (SPR) spectroscopy,[32–34] spectroscopic ellipsometry[27,29] and optical diffraction.[35] Interestingly, based on this property, an active tuning of the localized surface plasmon resonances could be achieved in hybrid SCO-coated gold nanostructures.[36,37] Conversely, it appears that the refractive index modulation of stimuli-responsive SCO materials also opens up interesting prospects for the development of practical applications based on refractive index sensing, such as gas sensors[37] or thin-film surface thermometers,[38,39] but also for manipulating light propagation in photonic devices.[40] However, the SCO materials used in most of these studies generally suffered from certain limitations, such as low environmental stability, weak cycling endurance, or a spin transition far from room temperature, which considerably restrained their possible integration into technologically relevant photonic devices.

In this context, recently, vacuum thermal deposited films of the compound $[Fe(HB(1,2,4\text{-triazol-1-yl})_3)_2]$ (**1**) have established a new benchmark in terms of robustness, reproducibility, film morphology, and SCO properties.[41] Spectrophotometric and ellipsometric investigations revealed that the SCO in films of **1** occurs at ≈64 °C and is associated with an abrupt and well-reversible drop of the refractive index in the UV–vis spectral range when switching from the LS (low-temperature) to the HS (high-temperature) state (see **Figure 1**).[29] While the refractive index modulation is relatively large in the UV range (associated with a notable change in the absorption properties of the material), temperature-dependent measurements (Figure 1b) reveal that Δn reaches ≈0.05 at 500 nm due to the sole SCO phenomenon. On the other hand, spectrophotometric measurements reveal that, apart from the relatively intense charge-transfer absorption bands observed in the UV spectral domain ($k = 0.15$ in the LS state at 320 nm), absorption and scattering losses remain very low in both spin states at any wavelength above 350 nm. More specifically, it is worth mentioning that complex **1** only exhibits a weak Laporte-forbidden ligand-field absorption band centered at ≈535 nm in the LS state associated with an absorption coefficient of $\alpha = 200$ cm^{-1} ($k = 9 \times 10^{-4}$), whereas no absorption bands arise at all in the HS state.[42] Therefore, in the whole visible spectral range, films of **1** shows a typical change of the refractive index of $\Delta n_{SCO} = 0.05$ upon the spin transition, while the extinction coefficient is extremely low and remains virtually unchanged in both spin states ($k < 10^{-3}$) (see also Figure S1, Supporting Information). This quite unusual behavior stems from the fact that the observed refractive index modulation in this spectral domain is not directly related to a change in the polarizability of the SCO material, but rather to the substantial modification of its unit-cell volume ($\Delta V/V = 4.5\%$) upon the spin transition,[43] as it can be expected through the empirical Gladstone-Dale relation: $\Delta n/(1-n) = \Delta V/V$.

Importantly, the SCO in films of **1** is known to be extremely well reproducible and reversible over more than ten million endurance cycles.[38] Moreover, the transition in **1** is volatile, which opens prospects for fast optical modulation.[42] Recently, these appealing assets have been exploited in the photonics context by inserting thin films of **1** into multilayer Ag/**1**/Ag Fabry-Pérot cavities.[29] Switching the SCO film from the LS to the HS state gave rise to a reversible blueshift of the cavity resonance (of up to 8 nm) in the visible domain, providing an initial proof for the spectral tunability conferred to the device by the SCO phenomenon.

In the present work, we harness the refractive index switching and the low extinction coefficient of films of **1** by designing a tunable optical resonator that consists of a metal-dielectric bilayer structure Ag (35 nm)/**1** (162 nm), excited using a coupling prism and operating in total internal reflection (TIR) geometry. We investigate numerically and experimentally the potential of this configuration to lead to a large spectral shift of the resonant optical modes and enhanced modulation of the reflectance contrast in the visible spectral range, as compared to previously studied

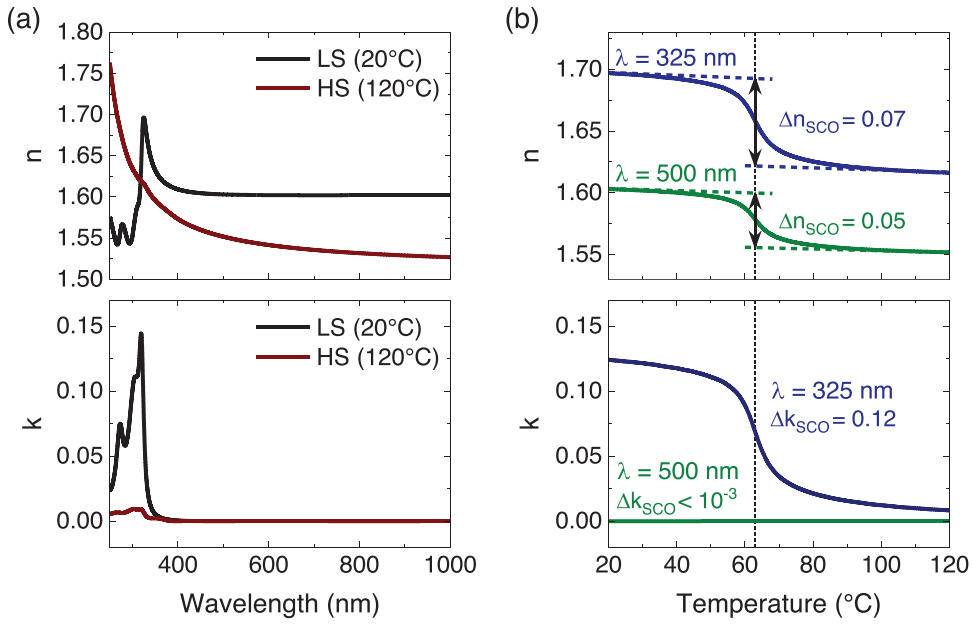

Figure 1. Optical properties of compound **1**. a) Real (*n*) and imaginary (*k*) part of the complex refractive index of **1** as a function of the wavelength in the LS (20 °C) and HS (120 °C) states. b) Evolution of *n* (top panel) and *k* (bottom panel) as a function of the temperature at two given wavelengths (325 and 500 nm). The vertical dashed line indicates the spin-transition temperature (64 °C).

SCO-based Fabry-Pérot cavities and other PCM-based resonators. In addition, using the high figures-of-merit of the present optical resonator in terms of thermo-optic tunability, photothermal nonlinearity and optical limiting applications are demonstrated.

2. Results and Discussion

2.1. Optical Properties and Thermal Tunability of the SCO-Based Resonator

Optical resonances in our Ag/SCO bilayers can be excited only under wavevector matching conditions, which we achieved using the Kretschmann method (see **Figure 2**a), employing a glass prism as a coupling medium.[44] One shall note that contrary to conventional SPR spectroscopy, the presence of the dielectric SCO layer (with a relatively large thickness, 162 nm) affords for the resonant excitation of electromagnetic modes with both TM (transverse magnetic; *p*) and TE (transverse electric; *s*) polarized light when passing through the glass prism under TIR conditions. Indeed, for a bare metallic film only a TM resonance can be excited, while the presence of an ultrathin dielectric coating merely leads to a shift of this resonance (either in wavelength or in angle, depending on the method of interrogation), which is the basis of the well-known SPR sensor applications. However, beyond a critical thickness of the dielectric layer, one can also observe a TE resonance, and upon a further increase in thickness, higher-order TE and TM resonances appear as well. In practice, coupling the incident light to the electromagnetic modes of the resonator thus gives rise to several sharp dips of the TIR intensity for different combinations of wavelength and angle of incidence, which fulfill the resonance conditions (i.e., simultaneous energy and wave vector matching).

A typical example of the resonance spectra obtained with our Ag (35 nm)/**1** (162 nm) bilayer structure is shown in Figure 2b at room temperature (25 °C) for various angles of incidence θ_{air}. In Figure 2b, spectra were recorded for both TE- and TM-polarized incoming light, allowing the results to be presented in terms of the ratio of these reflectances R_{TE}/R_{TM}. The obtained spectra show the existence of both TE and TM resonance modes, which appear, respectively, as dips and maxima in the R_{TE}/R_{TM} plots. Importantly, the film thicknesses were chosen (based on conventional transfer-matrix simulations) such that the TE resonance mode spans the visible wavelength region as the incidence angle varies over the 42–80° range.

Figure 2c,d show the overall reflectance (R_{TE}/R_{TM}) behavior of the Ag/**1** resonator obtained from experiments and transfer-matrix simulations, respectively, in the visible wavelength range (down to the silver plasma frequency at ≈320 nm) through the accessible range of TIR angles. These contour plots show the dispersion curves of both TE and TM resonance modes, depicted as dark blue and yellow bands, respectively. The simulated dispersion behavior closely matches the experimental one, albeit with considerably smaller linewidths. Indeed, by way of example, the experimental full width at half maximum (*FWHM*) of the TE resonance mode is found to be ≈37 nm (*Q*-factor = 12), which is much larger than the value predicted by the simulations (*FWHM* = 8 nm). This broadening of the resonances stems from multiple reasons. First, the calculations apply for electromagnetic plane waves, which remains a crude approximation for the large (≈5 mm diameter), roughly collimated white light beam used in the experiments. In addition, small inhomogeneities in the film thickness and surface/interface roughness result in an effective increase of the linewidths.

To investigate the temperature-dependent (and then SCO-dependent) properties of our optical resonator, the angle- and

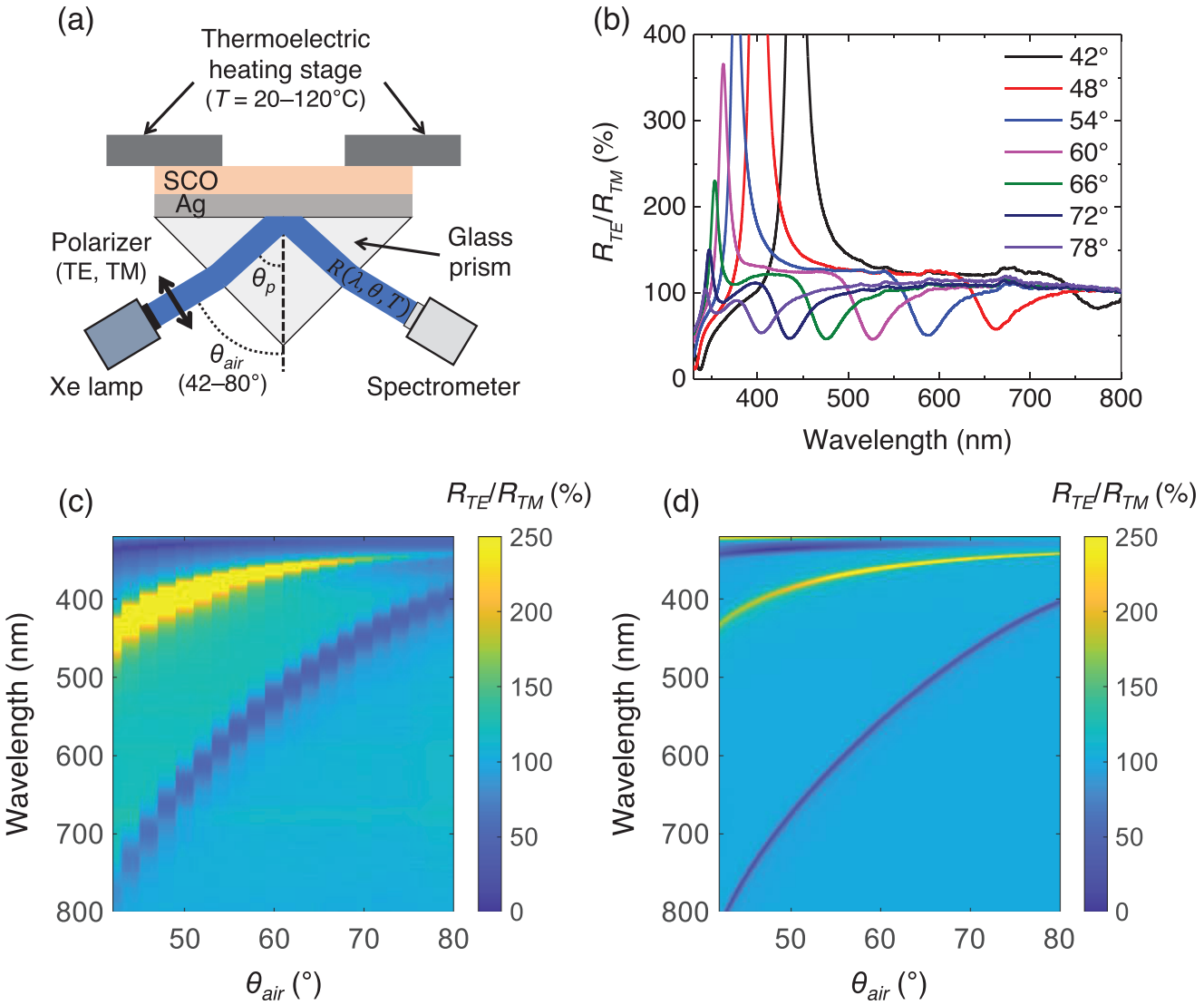

Figure 2. a) Scheme of the fabricated optical resonator, formed by an Ag (35 nm)/**1** (162 nm) bilayer structure deposited on a glass prism and excited using the Kretschmann method. b) Reflectance R_{TE}/R_{TM} spectra recorded at room temperature (25 °C, LS state) at different angles of incidence θ_{air}. Experimental c) and simulated d) angular dispersion of the optical resonator at 25 °C, showing both TE (dark-blue band) and TM (yellow band) resonant modes.

wavelength-dependent TE-polarized reflectance of the device was measured upon successive heating-cooling cycles between 25 and 120 °C. As shown in **Figure** 3a, within this temperature range, the angular dispersion of the TE resonance mode shows a significant shift between 60 and 80 °C, particularly at large incident angles. By way of an example, Figure 3b displays TE-polarized reflectance spectra of the resonator recorded at a fixed angle of incidence, $\theta_{air} = 68°$, for different selected temperatures. Importantly, we observe a sizeable blueshift (of up to 46 nm) of the resonance peak upon heating from 25 to 120 °C, which, interestingly, is found to be larger than the spectral linewidth of the optical mode ($FWHM$ = 37 nm). Besides, it is worth mentioning that most of this spectral shift occurs between 60 and 80 °C. The origin of this phenomenon becomes obvious in Figure 3c, which shows the detailed variation of the resonance wavelength as a function of temperature at the same angle of $\theta_{air} = 68°$. When heating the device from room temperature, one first observes a small linear blueshift of the resonance, followed by a more abrupt variation (with an inflection point at ≈70 °C) and, finally, a slow-down above ≈80 °C. Whereas the smooth linear resonance shifts at low and high temperatures denote ordinary thermoreflectance effects, the abrupt change can be unambiguously ascribed to the SCO phenomenon, which is well known to occur in films of **1** in this temperature range.[41] (Note that the temperature inflection point is found to be ≈6 °C higher than the transition temperature of films deposited on bare substrates, certainly due to the occurrence of a thermal lag arising from the large thermal inertia of the prism.) From these temperature measurements, one can thus clearly assess the resonance shift, $\Delta\lambda_{SCO}$ = 30 nm, which is associated solely with the spin-state switching without any background thermal effects. One may also notice that after the first heating, which is always somewhat anomalous due to "run-in"

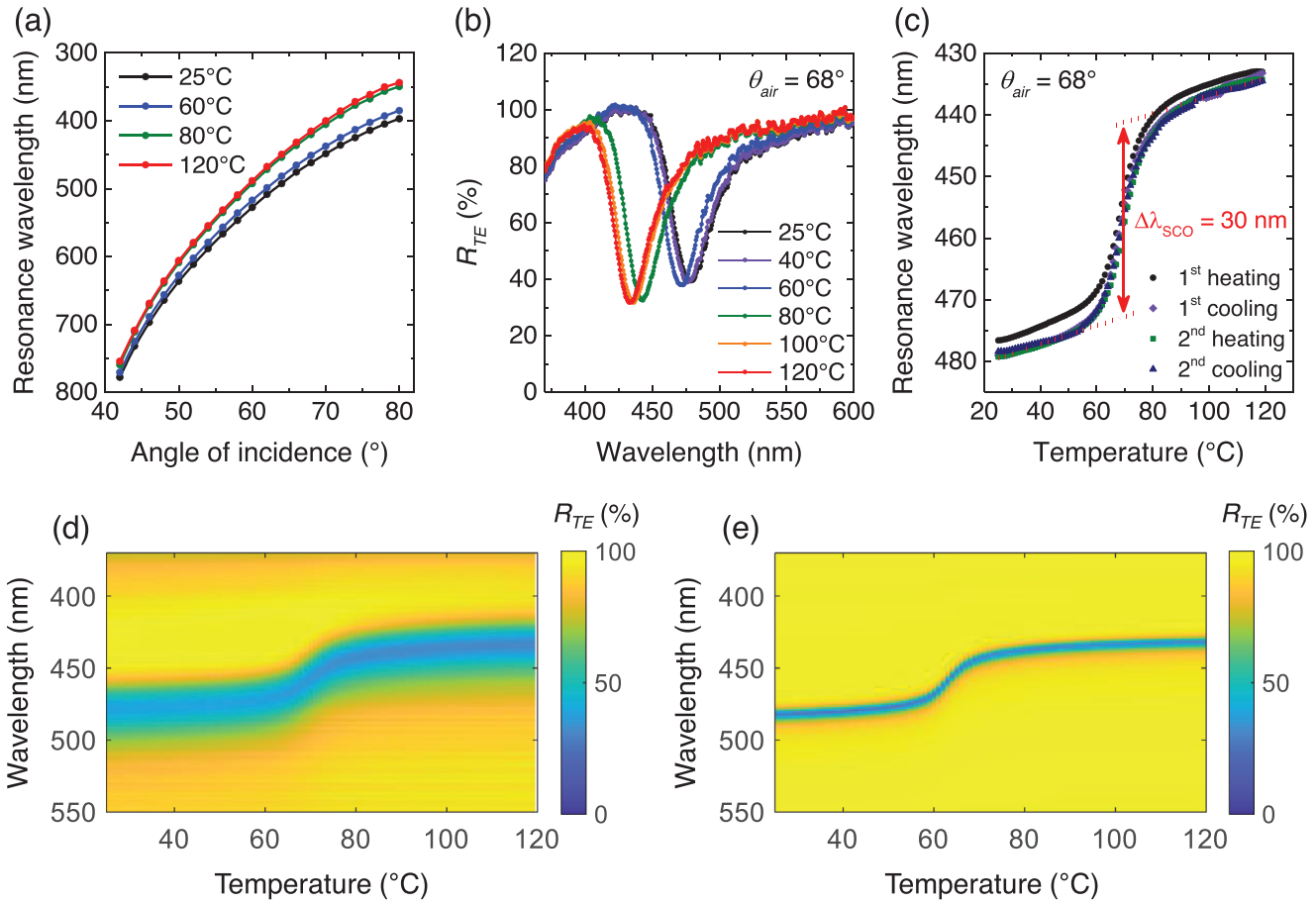

Figure 3. a) Angular dispersion curves of the Ag/**1** bilayer optical resonator acquired at selected temperatures (TE polarization). b) Reflectance spectra acquired at selected temperatures (TE polarization, $\theta_{air} = 68°$) showing the blueshift of the resonance peak upon the LS-to-HS transition. c) Temperature dependence of the resonance wavelength over the two first heating-cooling cycles (2 °C min^{-1}) undergone by the sample (TE polarization, $\theta_{air} = 68°$). Experimental d) and simulated e) wavelength-temperature maps of the reflectance, R_{TE}, of TE-polarized waves at an angle of incidence of $\theta_{air} = 68°$.

effects in the SCO film, the next heating-cooling curves overlap closely, denoting good reversibility of the resonance switching. It should be noted that subsequent thermal-cycling experiments were carried out on the same device after a period of 1 year of storage in ambient air (Figure S2, Supporting Information). These measurements confirm the good resilience of the SCO-based device (upon thermal cycling and storage in the air), even though a very slight decrease in $\Delta\lambda_{SCO}$ could be observed from ≈30 to ≈28 nm.

A more complete picture of the temperature dependence of the reflectance R_{TE} of the device is depicted in Figure 3d, from which we clearly observe that the SCO-induced shift of the resonance is comparable with the spectral linewidth, thus resulting in spectrally well-separated resonance peaks in the LS and HS states. Injecting the refractive index data presented in Figure 1 into the transfer-matrix calculations, the resonance shifts can be also reproduced in our numerical simulations with reasonably good accuracy (Figure 3e). One shall note, however, that a quantitative agreement between experiment and theory can be reached only if one takes into account both refractive index and film thickness changes accompanying the spin transition. Indeed, the decrease of the refractive index of films of **1** by $\Delta n_{SCO} = 0.05$ upon the LS-to-HS transition is expected to result in a 47-nm blueshift of the resonance wavelength, which significantly exceeds the experimentally observed value of 30 nm. However, concomitant with the refractive index change, the LS-to-HS switching also involves a substantial increase in the film thickness by ≈4.7%,[29] which partly counteracts the effect of Δn_{SCO}. Thus, if one also takes into account this volume change upon the spin transition, the simulations predict a 36-nm shift of the resonance wavelength (see Figure 3e), in fair agreement with the experiments.

Interestingly, the numerical simulations also reveal that the TE mode investigated in our experiments provides several advantages in comparison with the TM ones in the context of resonance tuning. Indeed, as depicted in **Figure 4**, TE resonances are, in general, narrower and exhibit a larger spectral shift at the SCO when compared to the TM modes. These differences are related (at least partly) to the fundamentally different electromagnetic field distributions associated with the two types of cavity modes. As discussed in refs.[45,46] for TM polarization, the electromagnetic field intensity is always high near the metal/dielectric interface, which gives rise to higher damping (associated with metal optical losses), whereas for TE polarization the field distribution peaks within the dielectric (SCO) layer thereby affording a higher

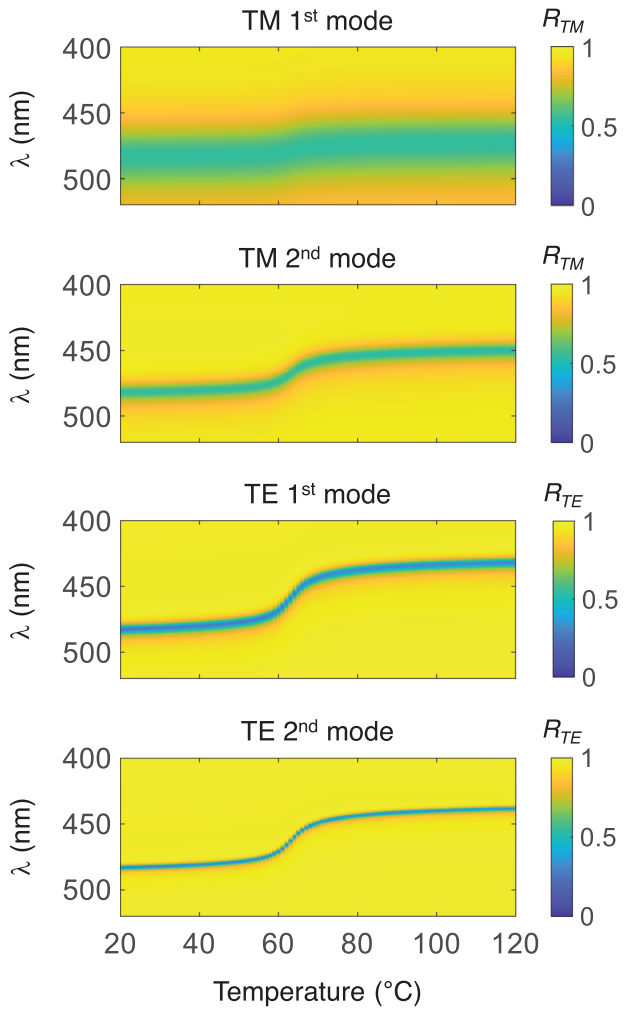

Figure 4. Temperature-dependent behavior of various simulated Ag/**1** devices displaying different types of resonances at ≈480 nm (in the LS state) for an angle of incidence of $\theta_{air} = 68°$. The thickness of the SCO layer was set to 31 nm (TM, 1st), 285 nm (TM, 2nd), 162 nm (TE, 1st) and 417 nm (TE, 2nd). The largest resonance shift (i.e., highest sensitivity to the refractive index change) upon the SCO is found for TE modes of the optical resonator.

sensitivity to the refractive index change. It is also interesting to note that, in our experiments, we investigate the first-order TE mode of the resonant structure, which leads to the largest spectral shift at the spin transition, but as displayed in Figure 4, our simulations show that higher-order TE resonances still provide high sensitivity with even narrower linewidths.

2.2. Figures-of-Merit of Our Thermally Tunable Optical Resonator

The shift of the resonance wavelength upon the SCO, $\Delta\lambda$, is an important characteristic of a thermally tunable optical device, but, from an applicative point of view, other important parameters must also be taken into account, such as the resonance linewidth ($FWHM$), the achievable reflectance (or transmittance) contrast at a given wavelength, ΔR, and the dependence of these different parameters on any temperature change. As a first figure-of-merit (FOM), **Figure 5a** (top panel) depicts the thermal evolution of the ratio $\Delta\lambda/FWHM$ ($\Delta\lambda$ being defined as $\Delta\lambda = \lambda - \lambda_{25\,°C}$) associated with the TE mode of our Ag/**1** resonator at an angle of incidence of 68°. While the total variation of $|\Delta\lambda|/FWHM$ over the whole temperature range [25–120 °C] reaches an absolute value of 1.22, a close inspection reveals that the sole SCO phenomenon induces a change by $|\Delta\lambda_{SCO}|/FWHM = 0.88$. This variation, close to unity, means that the SCO-induced spectral shift of the resonance is virtually comparable to the resonance linewidth, which is an important feature in achieving large optical contrast. Figure 5a (bottom panel) shows the thermal evolution of the derivative of $\Delta\lambda/FWHM$ with respect to the temperature, which characterizes the thermal spectral sensitivity of the device (always given at an angle of $\theta_{air} = 68°$). Far from the spin-transition temperature, $\Delta\lambda/FWHM$ decreases linearly with a rate of -4.5×10^{-3} °C^{-1}, but is then subject to a strong variation due to the SCO, indicating an increased gain in sensitivity. Indeed, close to the spin-transition temperature, the derivative of $\Delta\lambda/FWHM$ reaches a maximum value of -6.5×10^{-2} °C^{-1} (corresponding to a thermal variation of $\Delta\lambda$ with a maximum rate of $d(\Delta\lambda)/dT = -2.4$ nm °C^{-1}), which signifies that the thermal sensitivity of the device is multiplied by >10 near the transition temperature, in comparison with the spectral shift induced by ordinary thermal expansion.

Another important FOM concerns the achievable reflectance contrast of the device. As an example, Figure 5b (top panel) displays the temperature evolution of the reflectance change, $\Delta R = R - R_{25\,°C}$, measured for TE-polarized incoming light at an incident angle of 68° and a wavelength of $\lambda = 434$ nm. While the reflectance is virtually constant at low and high temperatures, we notice that most of the reflectance change takes place around the spin-transition temperature. Thus, utilizing our optical resonator at an angle of 68° and a wavelength of 434 nm, the SCO induces a (TE-polarized) reflectance change of up to 70%. The plot depicting the temperature evolution of $d(\Delta R)/dT$ (Figure 5b, bottom panel) shows that the spin-state switching involves a maximum thermal sensitivity, in terms of reflectance change, equal to −5.2% °C^{-1}, which is ≈2 orders of magnitude higher than the "ordinary" thermal sensitivity of the device.

The different figures-of-merit defined here to characterize the thermal tunability of the present optical resonator are substantially superior to those obtained in our previous work for the Ag/**1**/Ag multilayer Fabry–Pérot cavity, incorporating the same SCO material.[29] Indeed, in this latter cavity, we demonstrated a maximum shift of the TE resonance ($FWHM = 15$ nm, Q-factor = 30) of $\Delta\lambda_{SCO} = -5.5$ nm when going from the LS to the HS state, therefore implying a normalized spectral shift equal to $\Delta\lambda_{SCO}/FWHM = -0.37$, i.e., more than twice lower than that obtained in the present study. As for the optical contrast, the maximum reflectance change was found to be $\Delta R = 25\%$ (compared to 70% here). These differences come from the fact that, for a given refractive-index-changing material, the design of the optical resonator has great importance in achieving a high sensitivity to Δn. In the previously studied Ag/**1**/Ag Fabry-Pérot resonators, the cavity resonances did not show any discernible spectral shift at normal incidence ($k_{\parallel} = 0$) upon the SCO because the effect of Δn_{SCO} turns out to be fully counterbalanced by the concomitant expansion of the film thickness.[29] Thus, in

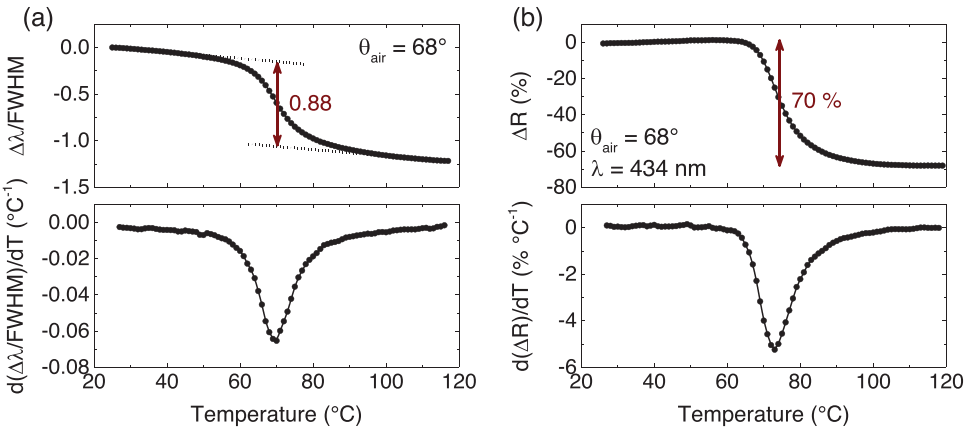

Figure 5. Main figures-of-merit of our Ag/**1** optical resonator. a) Thermal evolution of the ratio $\Delta\lambda/FWHM$ (top panel) and of its derivative with respect to the temperature (bottom panel), for the TE mode at an angle of incidence of 68°. b) Thermal evolution of the reflectance change ΔR (top panel) and of its derivative with respect to the temperature (bottom panel), at an incident angle of 68° and a wavelength of $\lambda = 434$ nm.

these cavities, the rather moderate spectral shift of −5.5 nm of the resonance peak could be observed only at large incidence angles ($\theta = 60°$), i.e., for sufficiently large values of the in-plane wave vector ($k_{\parallel} = 10.9\ \mu m^{-1}$). By contrast, in the present optical resonator, the use of a coupling prism enables optical modes with larger in-plane wave vectors to be excited ($k_{\parallel} = 17.7\ \mu m^{-1}$ at $\lambda = 500$ nm and $\theta_{air} = 68°$), making these optical modes more "sensitive" to the refractive index change of the SCO material.

Finally, in terms of switching speed, recent femtosecond optical spectroscopy investigations revealed that the (photo-)thermally induced switching dynamics of the SCO molecules fall in the order of tens of nanoseconds,[42] opening appealing perspectives for fast thermo-optical modulation. However, it is worth mentioning that the actual switching dynamics might be limited by the thermalization time (<1 µs)[38] of the nanometric thin films used (limited by the rather low thermal diffusivity of SCO materials), which should translate into a possible optical modulation in the MHz frequency range.

2.3. Comparison with Tunable Optical Resonators Integrating Other PCMs and Thermo-Optical Switches

To offer a perspective on the optical modulation performance of the above-reported SCO-based device, one might want to compare them with the characteristics of optical resonators incorporating other solid-solid PCMs, such as GST and VO_2. However, such a comparison turns out to be rather delicate since not only the design of the fabricated devices (microring resonators for the latter) and wavelength of operation (≈1550 nm) are different[6,10,47–50] but also because the principle of optical modulation is not the same since the phase change in GST or VO_2 involves *both* the switching of the real part of the PCM refractive index (phase modulation) and the change of the extinction coefficient (amplitude modulation). As a consequence, the shift of the resonance wavelength in GST- and VO_2-based resonators is also accompanied by a strong modification of the absorption losses and quality factor of the cavity. The situation is different in our SCO-based modulator, since the films of **1** exhibit negligible optical absorption losses ($k < 10^{-3}$) in both spin states, thus leaving the *Q*-factor unaffected by the SCO (see Figure 3b). Bearing in mind these fundamental differences, typical shifts of the resonance wavelength, $|\Delta\lambda|/FWHM$, within the range 0.5–0.8 were reported in the GST- and VO_2-based resonators,[6,49] which appears to be similar (and even smaller) to the one observed in our SCO-based device. On the other hand, in GST- and VO_2-based resonators, optical modulation depths greater than 10 dB are achieved,[6,48–50] at the expense of relatively large insertion losses of ≈2 dB (due to the residual optical absorption of the PCM, even in its low-absorbing phase), which, in turn, compromises the maximum transmittance (reflectance) change to ≈60%. In comparison, the optical modulation depth in our resonator is smaller (5.2 dB, since *R* varies from 100 to 30%), but the total variation of the reflectance is comparatively larger (70%) due to negligible insertion losses.

Arguably, the above-described SCO-based modulator can be also considered as an implementation of a thermo-optical switch. Indeed, the efficiency of the thermal tuning is primarily related to the so-called thermo-optic coefficient (TOC) of the material, dn/dT, which characterizes the response of the material's refractive index to any temperature changes. In thin films of **1**, the total change of the refractive index ($\Delta n_{SCO} = 0.05$) over a temperature range of $\Delta T = 20$ K centered around the transition temperature (see Figure 1b), gives rise to an average TOC of $\approx -2 \times 10^{-3}\ K^{-1}$ over this temperature window. (Note that this coefficient even reaches a maximum value of $-3.5 \times 10^{-3}\ K^{-1}$ at the spin-transition temperature, see Figure S3, Supporting Information.) This mean value is typically one to two orders of magnitude greater than that observed in other materials commonly used for thermo-optical switches (see **Table 1**). Beyond the TOC, a routinely used criterion for the optimization of thermo-optical switches[51–53] is the product of the power needed to thermally induce a shift of the optical phase by π, P_{π}, by the thermal time constant, τ. This metric turns out to be rather generic as P_{π} not only corresponds to the power needed to induce the full contrast change of Mach-Zehnder modulators but also to the power needed to shift the resonance of a device over its full free spectral range. In all cases, it has to be minimized to enable efficient and high-speed optical modulation. Expressing P_{π} and τ in terms of

Table 1. Comparison table of thermo-optical switches based on the figure-of-merit, $FOM = P_{\pi}\tau/(\lambda A)$.

Materials	$n \sim n_{eff}$	$\partial n_{eff}/\partial T$ [K^{-1}]	α_L [K^{-1}]	C_p [J g^{-1} K^{-1}]	ρ [g cm^{-3}]	$FOM \times 10^4$ [J cm^{-3}]	References
Si_3N_4	1.98 (1550 nm)	2.45×10^{-5}	2×10^{-6}	0.7	3.2	3.94	[54]
SiO_x	1.43 (1550 nm)	0.95×10^{-5}	0.55×10^{-6}	0.703	2.648	9.05	[54]
Polymethyl Methacrylate (PMMA)	1.49 (~600 nm)	-1.2×10^{-4}	7×10^{-5}	1.42	1.19	5.38	[55,56]
Polyurethane (PUR)	1.43 (~600 nm)	-4×10^{-4}	2×10^{-4}	2.44	1.1	1.18	[56]
GaN	2.38 (633 nm)	6.6×10^{-5}	5.6×10^{-6}	0.49	6.15	1.90	[57]
4H-SiC	2.65 (633 nm)	4.1×10^{-5}	4×10^{-6}	0.69	3.2	2.14	[57]
$LiTaO_3$	2.14 (633 nm)	-1.09×10^{-5}	1.6×10^{-5}	0.424	7.46	6.78	[58,59]
$BaTiO_3$	2.34 (660 nm)	1.8×10^{-4}	6×10^{-6}	0.434	6.02	0.67	[60,61]
SCO (compound **1**)	1.60 (500 nm)	-2×10^{-3}	2.2×10^{-3}	1.11	1.53	0.056	[62]

material-based parameters, while including the thermal expansion effect, leads to the following expression:[53]

$$P_{\pi}\tau = \frac{\lambda A \cdot C_p \rho}{2\left|\frac{\partial n_{\text{eff}}}{\partial T} + n_{\text{eff}}\alpha_{\text{L}}\right|} \quad (1)$$

where n_{eff} is the effective refractive index of propagation in the material, $\partial n_{\text{eff}}/\partial T$ is the thermo-optic coefficient, α_{L} is the thermal expansion coefficient, C_{p} is the specific heat capacity, ρ is the mass density, λ is the wavelength of operation, and A is the effective heated area. To draw out a fair comparison between the reported devices and the above-described structure, we have chosen to calculate the wavelength- and configuration-independent figure-of-merit, $FOM = P_{\pi}\tau/(\lambda A)$. As can be seen in Table 1, the optical modulator based on the above-used SCO compound (when operating close to its transition temperature) outperforms by a factor greater than 10 all the switches demonstrated so far.

2.4. Optical Limiting Application

In the following, we have taken advantage of the remarkable thermal tunability of our Ag/**1** bilayer resonator, to demonstrate its use for optical limiting applications in the visible spectral domain. Optical limiters are self-adaptive devices, that exhibit a specific input–output power response. Their response is linear (open state) below a threshold power, but for higher input powers, the output intensity rise slows down and becomes nearly constant (limiting state).[63,64] The main use of optical limiters is the protection of devices and humans against hazardous high-power light beams,[63] but they are also employed in optical computation and other domains,[65] wherever their nonlinear response function can provide benefit. In the present case, since the device under study embeds an absorbing metallic layer, it exhibits broadband self-heating upon (intense) visible excitation, which, in turn, induces a (power-dependent) modification of the reflection characteristics.

Experimentally, the power limiting performance of our optical resonator was characterized using a monochromatic laser beam ($\lambda = 532$ nm) for a series of incident laser powers between ≈1 and 60 mW, corresponding to power densities of up to 3 kW cm^{-2} (spot size of ≈50 µm). **Figure 6a** shows the angular reflectance spectra of our Ag/**1** device recorded at selected temperatures for low incident laser power, which basically reflects the same type of behavior as the wavelength spectra displayed in Figure 3b, i.e., a pronounced shift of the reflectance "dip" to lower angles when switching the SCO layer from the LS to the HS state. The device was then heated to 60 °C, i.e., only a few degrees Celsius below the spin-transition temperature, and the output optical power was recorded as a function of the input laser power for selected angles of incidence (shown by colored dots in Figure 6b on the angular spectrum measured at $T = 60$ °C). As displayed in Figure 6c, at a low angle (55°), the response is found to be linear, but for incident angles in the range 56–58°, a nonlinear behavior, characteristic of an optical limiting state, is clearly observed above a threshold input power so that the reflected laser power saturates at ≈10 mW. This phenomenon can be clearly linked to spin-state switching by tracing the evolution of the reflectance of the device as a function of the input power at the different incident angles (Figure 6d). Indeed, for θ_{air} = 56–58°, a sharp drop of the optical reflectance is observed when increasing the input laser intensity, with the result that the measured limiting power corresponds to the reflectance "dip" value (R_{TE} = 20–30%) obtained at the resonance. Finally, for higher angles of incidence (59–61°), the opposite behavior is observed: the reflected power is found to increase nonlinearly with the input power because the photothermally induced LS-to-HS transition induces a progressive increase of the reflectance, as evidenced in Figure 6d. For comparison, the same experiment performed at $T = 50$ °C, i.e., ≈14 °C below the spin-transition temperature, reveals a similar behavior (see

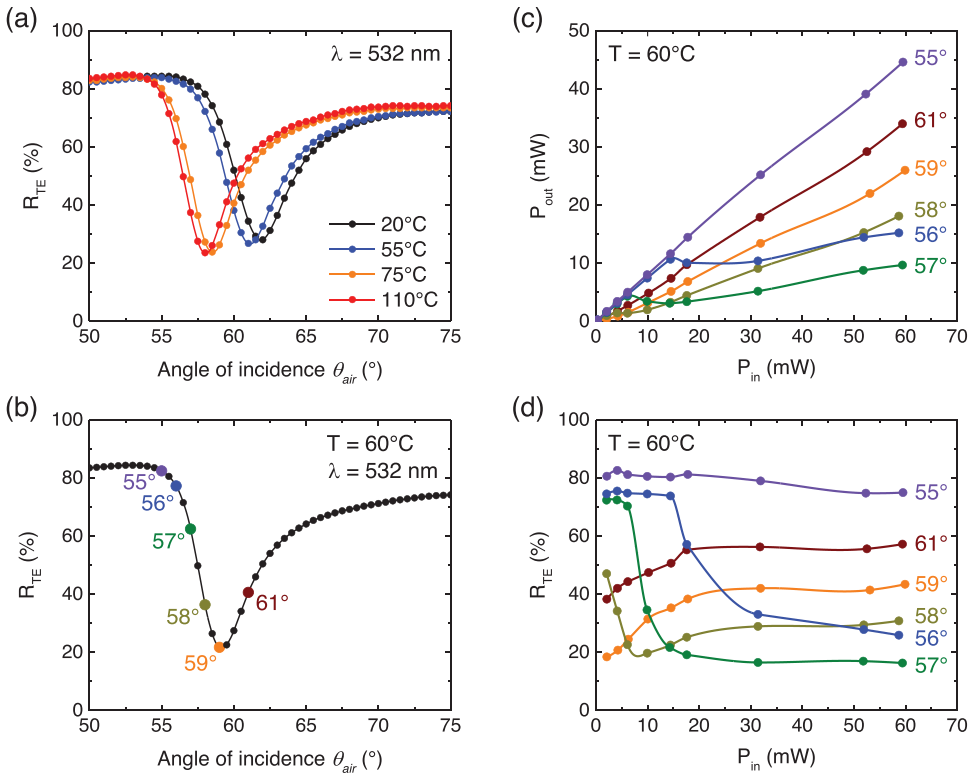

Figure 6. a) Angular reflectance spectra (TE polarization) of the Ag/**1** resonator recorded at low incident laser ($\lambda = 532$ nm) power at selected temperatures. b) Angular reflectance spectrum measured at $T = 60$ °C, displaying the experimental conditions (shown by colored dots) used for the optical limiting experiments. Reflected laser power c) and corresponding optical reflectance d) of the Ag/**1** device held at 60 °C as a function of the incident power measured at the different angles of incidence shown by colored dots in (b), revealing a nonlinear optical limiting behavior.

Figure S4, Supporting Information), with the exception that the optical limiting state is observed for comparatively higher threshold values of the incident laser power since more heating power is needed to thermally induce the transition from the LS to the HS state.

The observed optical limiting characteristics of our device for a continuous-wave excitation at an incident angle θ and a wavelength of operation λ can be deduced from the thermal dependence of the reflectance $R(\theta, \lambda, T)$ (calculated or measured at negligible incident power) through the relation $P_{out} = R(\theta, \lambda, T_a)P_{in}$, where T_a is the actual temperature of the device including the self-heating temperature rise induced by the incident power, P_{in}, starting from the substrate temperature T_{subs}. The former two quantities can, in fact, be related through the following expression:

$$R_{\text{th}} \times P_{\text{in}} = \int_{T_{\text{subs}}}^{T_a} \frac{dT}{1 - R(\theta, \lambda, T)} \tag{2}$$

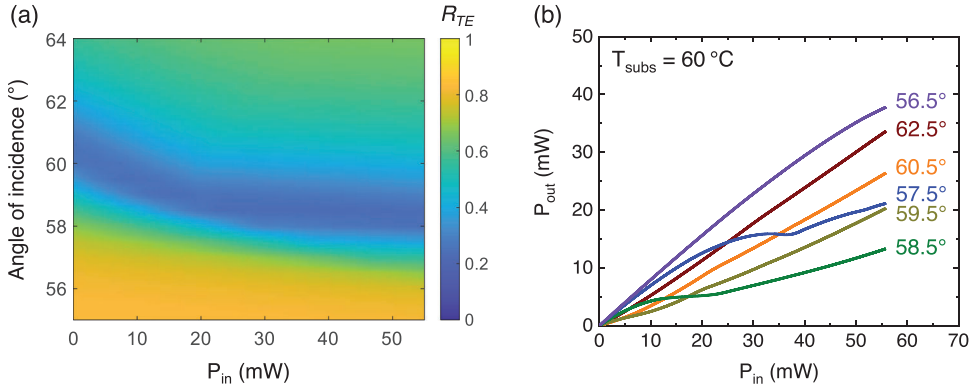

Figure 7. Nonlinear optical limiting characteristics of the Ag/**1** resonator calculated by transfer-matrix simulations at $\lambda = 532$ nm. a) Calculated power-angular map of the reflectance of the device (TE polarization) at $T_{subs} = 60$ °C and b) corresponding power transfer curves at selected angles of incidence, showing similar optical limiting behavior to the one observed experimentally.

where R_{th} is the thermal resistance of the device whose analytical formula is $R_{th} = 2/(\pi\kappa D)$ when the surface heat created by a uniform disk of diameter D is assumed to dissipate in a 1D manner over a semi-infinite substrate of thermal conductivity κ.[66] To simulate the optical limiting properties of our SCO-based resonator using transfer-matrix calculations, the thermo-angular reflectance map of the device was first reproduced at low incident laser power (see Figure S5, Supporting Information) for a wavelength of operation of 532 nm. Based on these simulations and using the above-mentioned set of equations (with $D = 50$ µm and $\kappa = 1.4$ W m^{-1} K^{-1} for the thermal conductivity of glass), the power-angular reflectance map of the optical resonator was calculated at $T_{subs} = 60$ °C (**Figure** 7a). As shown in Figure 7b, the corresponding power transfer curves obtained at selected angles of incidence confirm the existence of nonlinear optical limiting characteristics, for an appropriate choice of incidence angle and laser power, similar to the ones observed experimentally (Figure 6c).

3. Conclusion

The present work demonstrates the great potential of molecular spin-crossover nanomaterials in the perspective of using them as active elements in tunable optical devices. Taking advantage of the low extinction coefficient of complex **1** in both spin states, the SCO-based optical resonator fabricated here (designed to have a large modal overlap with the switchable molecular layer) allows to reach high figures-of-merit, in terms of resonance spectral shift ($\Delta\lambda_{SCO} = 30$ nm) and reflectance contrast tuning ($\Delta R = 70\%$). These characteristics are found to be comparable, or even superior, with respect to the performance reported for thermo-optical switches and well-established optical phase-change materials, with a major benefit which is the seamless device operation in the visible wavelength range. As a proof-of-concept, we demonstrated optical limiting properties at 532 nm, arising from the photothermal nonlinearity of the optical resonator, but, more generally, the present work also opens appealing scopes for other potential applications in which broadband optical transparency is mandatory.

4. Experimental Section

The microcrystalline powder of **1** was synthesized as described in ref.[43] and high-purity Ag was purchased from the company *NEYCO*. The hypotenuse face of a glass (N-BK7) right-angle prism was successively coated with a 35-nm-thick layer of Ag and a 162-nm-thick film of **1** by vacuum thermal evaporation at ≈5 × 10^{-7} Torr base pressure in a *PREVAC* system. To reach a high degree of crystallinity the as-deposited film of **1** was treated by water vapor annealing as described in ref.[41] The film thicknesses were monitored in situ using a quartz microbalance and verified ex situ using the optical reflectance data in combination with transfer-matrix calculations. The optical properties of the fabricated bilayer resonator were investigated by spectroscopic reflectometry measurements using a custom-built optical bench allowing the acquisition of reflectance data as a function of wavelength (200–1000 nm), incident angle (42–80°), light polarization, and temperature (20–120 °C) (see Figure 2a). A pulsed xenon lamp (Avalight-XE-HP, Avantes, 6 W, 150 Hz) is used as a white light source. The light beam is directed from the source to the sample by using fiber optics. Before reaching the sample, the light propagates through a collimating lens, a polarizer, and an iris diaphragm, allowing the control of the beam intensity and size. The sample is attached to a thermoelectric heating-cooling stage (PE120, Linkam Scientific) equipped with a center hole (in order to keep the air as the last dielectric layer), allowing for temperature scans at controlled rates (±2 °C min^{-1}). The reflected light is relayed to a spectrometer (Avaspec ULS2048CL-EVO-UA-50, Avantes, 2.5 nm spectral resolution) using an optical fiber (of core diameter 600 µm and numerical aperture NA = 0.22). The angles of incidence and collection are adjusted using two independent, high-precision rotation stages (position accuracy ≈1 mrad) driven by a microprocessor-controlled stepping motor (HDR50 and BSC202, Thorlabs). When the device was used in the optical limiting application, the photothermal heating of the device was achieved by means of a continuous, frequency-doubled Nd:YAG laser (532 nm, 100 mW), whose emission was focused on the bilayer resonator with a lens (of focal length, $f = 75$ mm) to a diameter of ≈50 µm. The incident and reflected laser powers were measured using a photodiode power sensor (S130C, Thorlabs).

The reflectivity spectra and angular dispersion of the Ag/**1** devices were simulated using conventional transfer-matrix calculations,[67] the resonator being modeled as a multilayer structure, which consists of semi-infinite space of glass, a layer of silver, a dielectric (SCO) layer and a semi-infinite space of air. The actual angles θ_p at which the incoming beam hits the Ag surface within the prism were obtained from the experimental incident angles in air, θ_{air}, taking into account the refraction of the light beam at the air-prism interface. Calculations were performed including the known optical properties of N-BK7 glass (using the Sellmeier equation) and silver.[68] The complex refractive index of compound **1** (Figure 1) was obtained by fitting temperature-dependent absorbance spectra measured by UV–vis spectrophotometry on a 150-nm-thick film of **1**, using a Drude–Lorentz oscillator model involving four Lorentz oscillators. Within this model, the value of n_{inf} (high-frequency part of the dielectric function) in the two spin states was extracted from previously reported temperature-dependent ellipsometric data.[29] This approach is compatible with satisfying the Kramers-Kronig relations. It should be noted, however, that the prime effect leading to the refractive index modulation in the visible range is the change in the film volume (or equivalently density), which is taken into account through the variation in n_{inf},[29] as a result of the Gladstone-Dale expression ($\Delta n/(1–n) = \Delta V/V$).

Supporting Information

Supporting Information is available from the Wiley Online Library or from the author.

Acknowledgements

This work received financial support from the Agence Nationale de la Recherche (project SCOPOL, ANR-22-CE09-0019), the University of Toulouse III (project AO Tremplin "MaCaPeSuMO"), and the Centre National de la Recherche Scientifique (project MITI "CMTS-SLM"). Part of the work was conducted at the LAAS-CNRS micro and nanotechnologies platform, which is a member of the French RENATECH network of cleanroom facilities. LZ and YZ thank the China Scholarship Council for a PhD grant.

Conflict of Interest

The authors declare no conflict of interest.

Data Availability Statement

The data that support the findings of this study are available from the corresponding author upon reasonable request.

Keywords

optical limiter, optical phase-change materials, refractive index modulation, spin-crossover materials, thermo-optical switches

Received: December 20, 2023
Revised: March 7, 2024
Published online:

[1] L. Kang, R. P. Jenkins, D. H. Werner, *Adv. Opt. Mater.* **2019**, *7*, 1801813.
[2] J. H. Ko, Y. J. Yoo, Y. Lee, H.-H. Jeong, Y. M. Song, *iScience* **2022**, *25*, 104727.
[3] U. Efron, I. Davidov, V. Sinelnikov, A. A. Friesem, in *Int. Symp. Optical Science Technology* SPIE, San Diego, CA **2001**.
[4] L. A. Coldren, S. W. Corzine, M. L. Mašanović, *Diode Lasers and Photonic Integrated Circuits*, Wiley, Hoboken, NJ **2012**.
[5] Z. Yang, C. Ko, S. Ramanathan, *Annu. Rev. Mater. Res.* **2011**, *41*, 337.
[6] J. D. Ryckman, V. Diez-Blanco, J. Nag, R. E. Marvel, B. K. Choi, R. F. Haglund, S. M. Weiss, *Opt. Express* **2012**, *20*, 13215.
[7] A. Karvounis, B. Gholipour, K. F. MacDonald, N. I. Zheludev, *Appl. Phys. Lett.* **2016**, *109*, 051103.
[8] M. Stegmaier, C. Ríos, H. Bhaskaran, W. H. P. Pernice, *ACS Photonics* **2016**, *3*, 828.
[9] K. J. Miller, K. A. Hallman, R. F. Haglund, S. M. Weiss, *Opt. Express* **2017**, *25*, 26527.
[10] K. J. Miller, R. F. Haglund, S. M. Weiss, *Opt. Mater. Express* **2018**, *8*, 2415.
[11] C. Williams, N. Hong, M. Julian, S. Borg, H. J. Kim, *Opt. Express* **2020**, *28*, 10583.
[12] P. Zuliani, E. Palumbo, M. Borghi, G. Dalla Libera, R. Annunziata, *Solid-State Electron.* **2015**, *111*, 27.
[13] M. Wuttig, H. Bhaskaran, T. Taubner, *Nat. Photonics* **2017**, *11*, 465.
[14] S. Raoux, W. Wełnic, D. Ielmini, *Chem. Rev.* **2010**, *110*, 240.
[15] H. Liu, J. Lu, X. R. Wang, *Nanotechnology* **2017**, *29*, 024002.
[16] Z. Yang, S. Ramanathan, *IEEE Photonics J* **2015**, *7*, 1.
[17] R. F. Haglund Jr., S. M. Weiss, K. Appavoo, in SPIE OPTO, SPIE, San Francisco, CA **2015**.
[18] R. E. Simpson, J. K. W. Yang, J. Hu, *Opt. Mater. Express* **2022**, *12*, 2368.
[19] W. Dong, H. Liu, J. K. Behera, L. Lu, R. J. H. Ng, K. V. Sreekanth, X. Zhou, J. K. W. Yang, R. E. Simpson, *Adv. Funct. Mater.* **2019**, *29*, 1806181.
[20] M. Delaney, I. Zeimpekis, D. Lawson, D. W. Hewak, O. L. Muskens, *Adv. Funct. Mater.* **2020**, *30*, 2002447.
[21] P. Gütlich, A. Hauser, H. Spiering, *Angew. Chem., Int. Ed.* **1994**, *33*, 2024.
[22] P. Gütlich, H. A. Goodwin, *Spin Crossover in Transition Metal Compounds I-III*, Springer-Verlag, Berlin, Heidelberg, **2004**.
[23] A. Bousseksou, G. Molnár, L. Salmon, W. Nicolazzi, *Chem. Soc. Rev.* **2011**, *40*, 3313.
[24] M. A. Halcrow, *Spin-Crossover Materials: Properties and Applications*, John Wiley & Sons, Ltd., Hoboken, NJ **2013**.
[25] K. Senthil Kumar, M. Ruben, *Coord. Chem. Rev.* **2017**, *346*, 176.
[26] A. Hauser, *Chem. Phys. Lett.* **1993**, *202*, 173.
[27] E. D. Loutete-Dangui, F. Varret, E. Codjovi, P. R. Dahoo, H. Tokoro, S. Ohkoshi, C. Eypert, J. F. Létard, J. M. Coanga, K. Boukheddaden, *Phys. Rev. B* **2007**, *75*, 184425.
[28] A. Iazzolino, G. Galle, J. Degert, J. F. Létard, E. Freysz, *Chem. Phys. Lett.* **2015**, *641*, 14.
[29] Y. Zhang, K. Ridier, V. Shalabaeva, I. Séguy, S. Pelloquin, H. Camon, S. Calvez, L. Routaboul, L. Salmon, G. Molnár, A. Bousseksou, *J. Mater. Chem. C* **2020**, *8*, 8007.
[30] G. Molnár, M. Mikolasek, K. Ridier, A. Fahs, W. Nicolazzi, A. Bousseksou, *Ann. Phys.* **2019**, *531*, 1900076.
[31] I. A. Gural'skiy, C. Quintero, K. Abdul-Kader, M. Lopes, C. Bartual-Murgui, L. Salmon, G. Molnár, A. Bousseksou, P. Zhao, D. Astruc, *J. Nanophotonics* **2012**, *6*, 063517.
[32] G. Félix, K. Abdul-Kader, T. Mahfoud, I. A. Gural'skiy, W. Nicolazzi, L. Salmon, G. Molnár, A. Bousseksou, *J. Am. Chem. Soc.* **2011**, *133*, 15342.
[33] A. Akou, C. Bartual-Murgui, K. Abdul-Kader, M. Lopes, G. Molnár, C. Thibault, C. Vieu, L. Salmon, A. Bousseksou, *Dalton Trans.* **2013**, *42*, 16021.
[34] S. Liu, K. Zhou, T. Yuan, W. Lei, H.-Y. Chen, X. Wang, W. Wang, *J. Am. Chem. Soc.* **2020**, *142*, 15852.
[35] A. Akou, I. A. Gural'skiy, L. Salmon, C. Bartual-Murgui, C. Thibault, C. Vieu, G. Molnár, A. Bousseksou, *J. Mater. Chem.* **2012**, *22*, 3752.
[36] K. Abdul-Kader, M. Lopes, C. Bartual-Murgui, O. Kraieva, E. M. Hernández, L. Salmon, W. Nicolazzi, F. Carcenac, C. Thibault, G. Molnár, A. Bousseksou, *Nanoscale* **2013**, *5*, 5288.
[37] C. Bartual-Murgui, A. Akou, C. Thibault, G. Molnár, C. Vieu, L. Salmon, A. Bousseksou, *J. Mater. Chem. C* **2015**, *3*, 1277.
[38] K. Ridier, A.-C. Bas, Y. Zhang, L. Routaboul, L. Salmon, G. Molnár, C. Bergaud, A. Bousseksou, *Nat. Commun.* **2020**, *11*, 3611.
[39] O. Y. Horniichuk, K. Ridier, L. Zhang, Y. Zhang, G. Molnár, L. Salmon, A. Bousseksou, *ACS Appl. Mater. Interfaces* **2022**, *14*, 52140.
[40] P. Mounaix, E. Freysz, J. Degert, N. Daro, J.-F. Létard, P. Kužel, V. Vigneras, L. Oyenhart, *Appl. Phys. Lett.* **2006**, *89*, 174105.
[41] V. Shalabaeva, S. Rat, M. D. Manrique-Juarez, A.-C. Bas, L. Vendier, L. Salmon, G. Molnár, A. Bousseksou, *J. Mater. Chem. C* **2017**, *5*, 4419.
[42] K. Ridier, A.-C. Bas, V. Shalabaeva, W. Nicolazzi, L. Salmon, G. Molnár, A. Bousseksou, M. Lorenc, R. Bertoni, E. Collet, H. Cailleau, *Adv. Mater.* **2019**, *31*, 1901361.
[43] S. Rat, K. Ridier, L. Vendier, G. Molnár, L. Salmon, A. Bousseksou, *Cryst.Eng.Comm.* **2017**, *19*, 3271.
[44] E. Kretschmann, H. Raether, *Z. Naturforsch. A* **1968**, *23*, 2135.
[45] H. E. de Bruijn, A. T. M. Lenferink, R. P. H. Kooyman, J. Greve, *Opt. Commun.* **1991**, *86*, 444.
[46] Z. Salamon, H. A. Macleod, G. Tollin, *Biophys. J.* **1997**, *73*, 2791.
[47] R. M. Briggs, I. M. Pryce, H. A. Atwater, *Opt. Express* **2010**, *18*, 11192.
[48] W. H. P. Pernice, H. Bhaskaran, *Appl. Phys. Lett.* **2012**, *101*, 171101.
[49] M. Rudé, J. Pello, R. E. Simpson, J. Osmond, G. Roelkens, J. J. G. M. van der Tol, V. Pruneri, *Appl. Phys. Lett.* **2013**, *103*, 141119.
[50] J. Zheng, A. Khanolkar, P. Xu, S. Colburn, S. Deshmukh, J. Myers, J. Frantz, E. Pop, J. Hendrickson, J. Doylend, N. Boechler, A. Majumdar, *Opt. Mater. Express* **2018**, *8*, 1551.
[51] M. R. Watts, J. Sun, C. DeRose, D. C. Trotter, R. W. Young, G. N. Nielson, *Opt. Lett.* **2013**, *38*, 733.
[52] N. C. Harris, Y. Ma, J. Mower, T. Baehr-Jones, D. Englund, M. Hochberg, C. Galland, *Opt. Express* **2014**, *22*, 10487.
[53] L.-Y. S. Chang, S. Pappert, P. K. L. Yu, *Opt. Lett.* **2023**, *48*, 1188.
[54] A. Arbabi, L. L. Goddard, *Opt. Lett.* **2013**, *38*, 3878.
[55] M. B. J. Diemeer, J. J. Brons, E. S. Trommel, *J. Light. Technol.* **1989**, *7*, 449.
[56] G. Coppola, L. Sirleto, I. Rendina, M. Iodice, *Opt. Eng.* **2011**, *50*, 071112.
[57] S. Rao, E. D. Mallemace, G. Cocorullo, G. Faggio, G. Messina, F. G. Della Corte, *Sci. Rep.* **2022**, *12*, 4809.
[58] G. Ghosh, *Opt. Lett.* **1994**, *19*, 1391.
[59] H. L. Saadon, N. Théofanous, M. Aillerie, M. D. Fontana, *Appl. Phys. B* **2006**, *83*, 609.
[60] Y. He, *Thermochim. Acta* **2004**, *419*, 135.
[61] A. Karvounis, F. Timpu, V. V. Vogler-Neuling, R. Savo, R. Grange, *Adv. Opt. Mater.* **2020**, *8*, 2001249.
[62] K. Ridier, S. Rat, H. J. Shepherd, L. Salmon, W. Nicolazzi, G. Molnár, A. Bousseksou, *Phys. Rev. B* **2017**, *96*, 134106.

[63] J. Parra, J. Navarro-Arenas, M. Menghini, M. Recaman, J. Pierre-Locquet, P. Sanchis, *APL Photonics* **2021**, *6*, 121301.
[64] C. Wan, Z. Zhang, J. Salman, J. King, Y. Xiao, Z. Yu, A. Shahsafi, R. Wambold, S. Ramanathan, M. A. Kats, *Laser Photonics Rev.* **2021**, *15*, 2100001.
[65] B. J. Shastri, A. N. Tait, T. Ferreira de Lima, W. H. P. Pernice, H. Bhaskaran, C. D. Wright, P. R. Prucnal, *Nat. Photonics* **2021**, *15*, 102.
[66] A. C. Tropper, S. Hoogland, *Prog. Quantum Electron.* **2006**, *30*, 1.
[67] C. C. Katsidis, D. I. Siapkas, *Appl. Opt.* **2002**, *41*, 3978.
[68] K. M. McPeak, S. V. Jayanti, S. J. P. Kress, S. Meyer, S. Iotti, A. Rossinelli, D. J. Norris, *ACS Photonics* **2015**, *2*, 326.